1 **Multiwavelength fluorescence lidar observations of smoke plumes**

2 Igor Veselovskii[1], Nikita Kasianik[1], Mikhail Korenskii[1], Qiaoyun Hu[2], Philippe Goloub[2], Thierry

3 Podvin[2], Dong Liu[3]

4 *[1]Prokhorov General Physics Institute of the Russian Academy of Sciences, Moscow, Russia.*

5 *[2]Univ. Lille, CNRS, UMR 8518 - LOA - Laboratoire d'Optique Atmosphérique, F-59650 Lille,*

6 *France*

7 *[3]State Key Laboratory of Modern Optical Instrumentation, College of Optical Science and*

8 *Engineering: International Research Center for Advanced Photonics, Zhejiang University,*

9 *Hangzhou 310027, China*

10   **Abstract**

11   A five-channel fluorescence lidar was developed for the study of atmospheric aerosol.

12 The fluorescence spectrum induced by 355 nm laser emission is analyzed in five spectral

13 intervals using interference filters. Central wavelengths and the widths of these five interference

14 filters are respectively: 438/29, 472/32, 513/29, 560/40 and 614/54 nm. The relative calibration

15 of these channels has been performed using a tungsten-halogen lamp with color temperature

16 2800K. This new lidar system was operated during Summer – Autumn 2022, when strong forest

17 fires occurred in the Moscow region and generated a series of smoke plumes analyzed in this

18 study. Our results demonstrate that, for urban aerosol, the maximal fluorescence backscattering

19 is observed in 472 nm channel. For the smoke the maximum is shifted toward longer

20 wavelengths, and the fluorescence backscattering coefficients in 472 nm, 513 nm and 560 nm

21 channels have comparable value. Thus, from the analysis of the ratios of fluorescence

22 backscattering in available channels, we show that it is possible to identify smoke layers. The

23 particle classification based on single channel fluorescence capacity (ratio of the fluorescence

24 backscattering to elastic one), has limitations at high relative humidity (RH). The fluorescence

25 capacity is indeed decreasing when water uptake of particles enhances the elastic scattering.

26 However, the spectral variation of fluorescence backscattering does not exhibit any dependence

27 on RH and can be therefore applied for aerosol identification.

28

29   **1. Introduction**

30   The knowledge of the chemical composition of atmospheric aerosol is important for

31 characterization of its impact on the Earth radiation balance (Boucher et al., 2013; IPCC 2022).

The composition of aerosol, however, is strongly variable, and in practice, several general aerosol types are considered usually based on their origin (Dubovik et al., 2002). The Mie-Raman and high spectral resolution lidars provide the opportunity to derive vertical distribution of the particle extinction and backscattering coefficients together with multispectral depolarization ratio. The main aerosol types can be distinguished based on such observations (Burton et al., 2012, 2013; Groß et al., 2013; Mamouri et al., 2017; Papagiannopoulos et al., 2018; Nicolae et al., 2018; Hara et al., 2018; Wang et al., 2021; Mylonaki et al., 2021). However, due to the variability of the aerosol parameters, the particle intensive properties (properties that are independent of concentration), such as lidar ratios, depolarization ratios and Angstrom exponents can vary in a wide range, even for aerosols from the same origin, which complicates their identification.

The fluorescence measurements provide new independent information about aerosol composition, which can be used for classification. (Veselovskii et al., 2022b). Being induced by 355 nm laser radiation the atmospheric fluorescence emission spreads in a wide spectral range from approximately 380 nm to beyond 700 nm. The multianode photomultipliers combined with spectrometer, in principle, allow the profiling of the full fluorescence spectrum (Sugimoto et al., 2012; Saito et al., 2022; Reichardt et al., 2022). In a more simple approach a single fluorescence channel has been integrated into existing multiwavelength Mie-Raman lidar (Veselovskii et al., 2020), and a fraction of the fluorescence spectrum is selected by a wideband interference filter. High transmittance of modern interference filters (above 95%), allows efficient detection of fluorescence emission, and when combined with simultaneous depolarization measurements the main aerosol types, such as dust, smoke, pollen and urban aerosols can be identified (Veselovskii et al., 2022b). This classification scheme relies on the fluorescence capacity G_λ, which is the ratio of fluorescence backscattering to elastic backscattering at laser wavelength. The fluorescence capacity, however, depends on the relative humidity (RH), because enhanced elastic backscattering leads to decrease of G_λ (Veselovskii et al., 2021). As a result, at high RH, we cannot discern unambiguously whether the decrease of G_λ comes from water uptake or from changes in the aerosol composition.

The water uptake increases the elastic backscattering but normally does not alter the chemical components and consequently the total amount of fluorescent molecules within a particle does not change. The illumination intensity distribution within a particle, as well as the

63   emission angular distribution can be altered by the change of particle size and refractive index

64   during the hygroscopic growth. However, this effect occurs for relatively big microspheres with

65   size parameter exceeding approximately 10 (Veselovskii et al., 2002). Thus, fluorescence of the

66   fine mode particles should be less influenced by the hygroscopic growth. Our existing lidar data-

67   base in well mixed boundary layer situations demonstrate that, at least, for urban and smoke

68   particles, the fluorescence backscattering coefficient did not change during water uptake. Thus,

69   we have good reason to expect, that fluorescence spectrum is not modified by the aerosol

70   hygroscopic growth, and several fluorescence channels should provide more reliable information

71   upon aerosol type.

72   Smoke is one of the most abundant aerosol types and it was intensively studied with Mie-

73   Raman lidars for decades (Adam et al., 2020 and references therein). Smoke is characterized also

74   by high fluorescence capacity (probably due to the presence of the organic carbon fraction), thus

75   fluorescence lidar measurements proved to be very efficient for smoke identification and analysis

76   (Hu et al., 2022, Veselovskii et al., 2022a,b). However, as mentioned, at high RH levels, the

77   classification of smoke, based on a single channel fluorescence may fail. The solution could be

78   the detection of fluorescence at several wavelengths. In July 2022 a new lidar system equipped

79   with five fluorescence channels, was assembled in Prokhorov General Physics Institute, Troitsk,

80   Moscow. The lidar was in operation during Summer and Autumn 2022, when strong forest fires

81   occurred in the Moscow region. In this paper we analyze the spectral dependence of the

82   fluorescence backscattering inside and outside the smoke plumes. The results demonstrate that

83   the hygroscopic growth does not affect the spectral dependence of fluorescence backscattering.

84

85   ## 2. Experimental setup

86   The fluorescence lidar is based on a tripled Nd:YAG laser with pulse energy of 80 mJ at

87   355 nm and repetition rate of 20 Hz. Backscattered light is collected by a 40 cm aperture

88   Newtonian telescope and the lidar signals are digitized with Licel transient recorders with 7.5 m

89   range resolution, allowing simultaneous detection in the analog and photon counting modes. The

90   optical scheme of the receiving module is presented in Fig.1. The system is designed to detect

91   elastic backscattering at 355 nm, nitrogen Raman backscattering at 387 nm and fluorescence

92   backscattering in five spectral intervals. These intervals are separated with dichroic beamsplitters

93   and isolated by the interference filters manufactured by Alluxa. The central wavelengths and the

widths of transmission bands (FWHM) of these fluorescence channels are respectively: 438/29, 472/32, 513/29, 560/40 and 614/54 nm. The transmission of the filters exceeds 97%, while suppression of optical signal out of band is above OD6. To improve the suppression of elastic backscattering we installed two filters in tandem in every channel.

Laser radiation at 532 nm can induce additional aerosol fluorescence which will contaminate long-wave channels. To remove this potential contamination, the emissions at 532 nm and 1064 nm are separated with dichroic mirrors and redirected to an optical dump. Therefore, the laser beam sent into the atmosphere has only one wavelength - 355 nm. As follows from Fig.1, the 532 nm radiation is out of the transmission band of the filters, which prevents the leaking of residual 532 nm component to the fluorescence channels. We should mention, that the vibrational overtone of N_2 Raman scattering at 424.4 nm is within the transmission band of 438 nm channel. In accordance with results of Knippers et al. (1985), Raman intensity of this overtone is about three orders lower than intensity of N_2 fundamental vibration (for 488 nm laser wavelength). Based on our measurements, contribution of N_2 overtone to fluorescence signal from urban aerosol (with backscattering coefficient of 1.0 $Mm^{-1}sr^{-1}$ at 355 nm and $G_{438}=0.3\times10^{-4}$) is estimated to be below 5% at 1000 m height. In all the channels the PMTs R9880U-01 were used, except in the 614 nm channel, where R9880-20 PMT was installed, due to its higher sensitivity in the red spectral region. The strong sunlight background at daytime restricts the fluorescence observations to only nighttime. All the observations presented in this study were performed at 45 degree angle to horizon.

The aerosol extinction coefficient at 355 nm (α_{355}) was calculated from Raman observations as described in Ansmann et al., (1992). For the calculation of the backscattering coefficient β_{355} in the presence of clouds, we used approach described in Veselovskii et al. (2022b). Additional information about atmospheric properties was available from radiosonde measurements at Dolgoprudnyi station, located about 50 km away from the observation site. It should be mentioned that the current lidar configuration does not allow measurement of the depolarization ratio.

The fluorescence backscattering coefficient $\beta_{F\lambda}$ is calculated from the ratio of fluorescence signal to 387 nm nitrogen Raman signal with correction for differential Raleigh and aerosol extinction, as described in Veselovskii et al. (2020). The atmospheric transmission of fluorescence signal is calculated for the wavelengths corresponding to the center of the filter

transmission band. The error due to the neglect of spectral dependence of the Raleigh extinction inside the filter transmission band is the largest for the shortwave channel (438 nm). Computations show that at height of 4000 m corresponding error of β_{F438} is below 4%. For correction of errors provided by the aerosol differential extinction we need to make an assumption about the value of the extinction Angstrom exponent (EAE). In particular, for the aged smoke the EAE for 355/532 nm wavelengths is about 1.0 (Hu et al., 2022) and this value was used in the data analysis in our study. The uncertainties, due to possible deviation of EAE from 1.0 value are analyzed in section 3.1 of this paper.

For calculation of $\beta_{F\lambda}$ one needs to know the differential cross section of nitrogen Raman scattering, σ_R, and the relative sensitivity of the nitrogen and fluorescence detection channels. The value σ_R=2.744*10^{-30} cm^{2}sr^{-1} at 355 nm was taken from Venable et al. (2011). Sensitivity of R9880U-01 photocathode in the 387 nm - 438 nm range varies for less than 10%, so we neglect this variation and calculate relative sensitivity of the PMTs as described in Veselovskii et al. (2020). The relative sensitivity of the rest of the fluorescence channels in respect to the 438 nm one, was calculated from laboratory measurements using a tungsten-halogen lamp Thorlabs QTH10/M with color temperature 2800K as a source, assuming this source follows the Planck blackbody emission. For calibration, the telescope is installed horizontally and the lamp is placed at a distance of 4 m from the entrance. The screen, installed in front of the telescope, selected the central part of the lamp radiation of 50 mm diameter, which was used for calibration. This procedure was performed once a week and variations of the calibration coefficients during August-September 2022 period were below 15% for the 614 nm channel and below 10% for the rest of the channels. Thus, the uncertainties of $\beta_{F\lambda}$ calculation include the systematical errors of calibration procedure (ε_{cal}), the errors due to indeterminacy of the choice of the Angstrom exponent (ε_A), and the statistical errors of the measurements (ε_{st}). For the vertical profiles of the fluorescence backscattering in section 3, we do not provide the systematical errors of the calibration, however, ε_{cal} are considered, when the spectra of the fluorescence backscattering are analyzed.

One should note that $\beta_{F\lambda}$ is the integral of fluorescence backscattering over the filter transmission band D_λ. To compare $\beta_{F\lambda}$ at different fluorescence channels we compute the mean backscattering coefficients per elementary spectral interval, $B_\lambda = \dfrac{\beta_{F\lambda}}{D_\lambda}$, denoted as "fluorescence

155 spectral backscattering coefficient". The fluorescence capacity G_λ, which is the ratio of the

156 fluorescence backscattering to the elastic one, in principle, can be calculated for any laser

157 wavelength. In our previous studies we calculated G_λ with respect to β_{532}, however, in this work,

158 it was calculated with respect to 355 nm $G_\lambda = \dfrac{\beta_{F\lambda}}{\beta_{355}}$, since 532 nm wavelength was not available.

159 All $\beta_{F\lambda}$, G_λ and B_λ profiles presented in this work were smoothed with the Savitzky – Golay

160 method, using a second order polynomial with 7 points in the window.

161

162 **3.   Measurements and analysis**

163 In August 2022 numerous smoke layers originating from the forest fires in Ryazan region

164 (about 160 km South – East of Moscow) were detcted over the lidar station. The travel time of

165 the layers was less than two days, thus smoke can be considered as fresh. The previous

166 fluorescence studies of smoke plumes transported over Atlantic and including 466/44 nm

167 fluorescence measurements revealed that fluorescence capacity (calculated for β_{532}), in the

168 absence of hygroscopic growth, varied within the range $(2.5–5.0)\times10^{-4}$ (Veselovskii et al., 2021,

169 2022a,b; Hu et al., 2022). The Backscattering Angstrom Exponent (BAE) of smoke for 355/532

170 nm wavelengths, is about 2.0, and fluorescence capacity G_{472} in 472/32 nm channel (calculated

171 for β_{355} from past studies) is expected to be in the range $(0.8–1.6)\times10^{-4}$. Here and below the

172 fluorescence capacity will be provided for 472 nm, because in most of the cases the fluorescence

173 in this channel was maximal.

174

175 **3.1.   Fluorescence measurements during smoke episode**

176 ***27-28 August 2022***

177 Two-day backward trajectories from the NOAA HYSPLIT model for the air mass reaching

178 Moscow on 28 August at 00:00 UTC are shown in Fig.2. Air masses observed at 1500 m, passed

179 over the fire region, close to the ground, and should thus contain biomass burning aerosols. The

180 relative humidity measured by the radiosonde, at 00:00 UTC, was about 35% at 1000 m and

181 increased with height up to 70% at 3000 m. Temporal evolution of the aerosol backscattering

182 coefficient, β_{355}, fluorescence backscattering, β_{F472}, and fluorescence capacity, G_{472}, are shown in

183 Fig.3. Aerosols are localized mainly below 3000 m, while above 4000 m cloud layers can be

184 seen. The highest fluorescence backscattering values were encountered before 20:30 UTC inside

185 the boundary layer. The fluorescence capacity exceeds 2.5×10^{-4}, which is the highest G_{472}

186 observed in our measurements. After 20:30 G_{472} decreases but remains above 1.0×10^{-4}, which, in

187 principle, can be due to mixing of smoke with urban aerosol.

188   Vertical profiles of the fluorescence spectral backscattering coefficients B_λ are shown in

189 Fig.4a for the period that exhibited the highest fluorescence capacity (19:00-20:00 UTC). The

190 profiles of B_{472}, B_{513}, B_{560} are similar, and the ratios B_{472}/B_{513}, B_{472}/B_{560} in Fig.4b are close to 1.0..

191 The fluorescence capacity G_{472} is above 2.0×10^{-4}, in 1.0 km – 2.5 km height range, where β_{355}

192 and B_λ are maximal. To quantify the uncertainty due to indeterminacy of the EAE choice, the

193 Fig.4c shows profiles of B_{472}, B_{614} and the ratios B_{472}/B_{513}, B_{472}/B_{614} calculated for values of EAE

194 A=0.5, 1.0, 1.5. The optical depth at 355 nm exceeded 0.55 at 3000 m height. The aerosol

195 differential extinction provides the largest effect to B_{614}, and the difference between values

196 obtained with A=1.0 and 1.5 at 3000 m is about 6.5%. For B_{472} this difference is lower, about

197 5%. However, for the ratios of fluorescence backscattering, the influence of aerosol is lower: for

198 both B_{472}/B_{513} and B_{472}/B_{614} corresponding difference is below 2.0%.

199   Fluorescence spectra of two distinct temporal intervals can be seen in Fig.5. In the interval

200 corresponding to high fluorescence capacity (19:00-20:00 UTC), the maximum fluorescence

201 backscattering is observed in 513 nm channel, which agrees with the spectrum of smoke

202 fluorescence provided by Reichard et al. (2022). In the second interval (23:00-01:00 UTC), when

203 fluorescence capacity is lower, the fluorescence is maximal at 472 nm and at longer wavelengths

204 it decreases fast. The lidar ratios (S_{355}) for both time intervals are shown in the same figure. For

205 the first interval (with maximum G_{472}) S_{355} is about 60 sr, while for the second interval S_{355}

206 decreases to about 40 sr. The highest spectral fluorescence capacity of smoke (capacity per

207 elementary spectral interval), reported by Reichard et al. (2022) for 455–535 nm range is about

208 8×10^{-6} nm^{-1}. This is very comparable with our value (11×10^{-6} nm^{-1}) calculated from data plotted

209 in Fig.4 and 5 at 472 nm in the 19:00-20:00 UTC time interval.

210   The variation of the fluorescence spectra is revealed by the ratio of the fluorescence

211 backscattering coefficients at different wavelengths (e.g. B_{472}/B_λ). In particular, inside the aerosol

212 plume in Fig.3 B_λ does not change significantly in 472 – 560 nm range, and the ratios B_{472}/B_{513},

213 B_{472}/B_{560} are close to 1.0. Spatio-temporal evolution of these ratios is shown in the right column

214 in Fig.3. The intervals with the maximum G_{472} are well distinguished by minimum B_{472}/B_{513} and

215 B_{472}/B_{560} ratios. At the same time, ratio B_{472}/B_{438} appears to be less sensitive to G_{472} changes.

216 Actually, this ratio even increases inside the aerosol plume. Thus, the analysis of Fig.3 reveals

217 two types of the particles. The first type having a high fluorescence capacity ($G_{472}>2.0\times10^{-4}$) and

218 a lidar ratio close to 60 sr can be classified as "pure" smoke. The second type, with lower

219 fluorescence capacity ($G_{472}\sim1\times10^{-4}$) and a smaller lidar ratio, can be a mixture of smoke and

220 urban aerosol.

221 Forest fires stopped in the beginning of September, so during September – October the

222 urban aerosols were predominant. Fig.6 shows corresponding fluorescence spectra, normalized

223 to B_{472}. Measurements were performed during 07:00-09:00 UTC and averaged within the

224 boundary layer between 500 m and 1000 m. For urban aerosols, fluorescence at wavelengths

225 larger than 472 nm decreases fast. Presence of remaining smoke, however, may lead to some

226 increase of B_λ in the $513 - 614$ nm interval. For urban aerosol particles the fluorescence capacity

227 G_{472} for urban particles varied within $(0.1\text{-}0.4)\times10^{-4}$ and the lidar ratios within 30-50 sr interval.

228 Thus, mixing of smoke and urban particles can explain the variability observed in fluorescence

229 spectrum on Fig.5.

230

231 ***17 August 2022***

232 The spatio – temporal intervals with high fluorescence capacity were observed also for

233 other days. On August 17-18, 2022 between $18:00 - 19:00$ UTC, fluorescence capacity at 472

234 nm, the G_{472}, within the aerosol plume increased above 1.0×10^{-4} (Fig.7). Simultaneously, the

235 ratio B_{472}/B_{560} decreases to less than 0.8. Outside the plume, the fluorescence capacity is (0.4-

236 $0.7)\times10^{-4}$ and the ratio B_{472}/B_{560} increases up to 1.2. Corresponding fluorescence spectra are

237 shown in Fig.8. Inside the plume the fluorescence is maximal in the 560 nm channel, while

238 outside the maximum is shifted to 472 nm. Similarly to the 27-28 August event (Fig.5), the lidar

239 ratio S_{355} is about 60 sr inside the plume and decreases down to about 30 sr outside the plume.

240 Thus, again, we conclude that in the interval having the highest G_{472}, smoke particles are

241 predominant, while outside we very likely addressed a mixture of smoke and urban aerosol.

242

243 **3.2.   Analysis of fluorescence profiles observed in the presence of hygroscopic**

244 **growth of aerosol**.

245 Our previous studies with a single channel fluorescence lidar revealed, that the

246 hygroscopic growth of aerosol particles decreases the fluorescence capacity, but does not affect

247   the fluorescence backscattering coefficient (Veselovskii et all, 2021). Thus, when fluorescence
248   spectra are available, one can expect that spectral dependence of fluorescence backscattering
249   coefficients will preserve information about particle type (will not be influenced by water
250   uptake). Below, we provide interpretation of the measurements performed during the nights
251   August 21-22 and 23-24 2022. In both cases, RH increased with altitude and the hygroscopic
252   growth is one possible contributor to the observed increase of particle backscattering coefficient.
253   Our results show, that on August 21-22 the shape of the fluorescence spectrum (the set of B_λ/B_{472}
254   ratios) did not exhibit any change with altitude, whereas, conversely, on August 23-24 the shape
255   of the fluorescence spectrum has changed with altitude, indicating possible change of aerosol
256   composition with height.

257   Fig.9. shows vertical profiles of the fluorescence spectral backscattering coefficients, B_λ,
258   together with backscattering β_{355} coefficient, fluorescence capacity G_{472}, and B_{472}/B_{438}, B_{472}/B_{513},
259   B_{472}/B_{560} ratios on August 21 2022. Profiles of B_{472}/B_{614} ratio are noisier and not used for
260   analysis. The profile of relative humidity measured by a radiosonde at Dolgoprudnyi station,
261   shows increase of RH with altitude from 30% to 80% within 1000-4500 interval. Inside 3000-
262   4000 m range, the fluorescence backscattering does not demonstrate significant variations while
263   elastic backscattering increases by two orders of magnitude (from approximately 1 $Mm^{-1}sr^{-1}$ to
264   100 $Mm^{-1}sr^{-1}$), which should be attributed to aerosol hygroscopic growth. The fluorescence
265   capacity, G_{472}, decreases to less than 0.01×10^{-4} at 4000 m, however, the ratios B_{472}/B_{438},
266   B_{472}/B_{513}, B_{472}/B_{560} do not change with altitude, meaning that i) the spectrum (its shape) is not
267   affected by water uptake process and that ii) aerosol composition remains constant.

268   Temporal evolution of the particle parameters on the August 23-24 night is presented in
269   Fig.10. The relative humidity increases with height and during 18:00-20:00 time interval a cloud
270   was formed at ~3000 m. After 20:00 the fluorescence capacity inside 2000-3000 m height range
271   is low (below 0.2×10^{-4}), however low values of G_{472} can also be explained by particle
272   hygroscopic growth, thus one can not yet conclude that aerosol composition has changed,
273   because the two effects (RH + aerosol changes) can occur simultaneously. Meanwhile, B_{472}/B_{560}
274   ratio decreases above 2000 m, which can be an indication of aerosol composition change.
275   Profiles of aerosol properties for the time interval 20:30-23:30 are shown in Fig.11. In
276   accordance with the radiosonde measurements the relative humidity reaches 80% at 3000 m at
277   00:00 UTC. At 1000 m height, where RH is low (~35%), G_{472} is about 0.4×10^{-4}, hence, urban

278   aerosol type is predominant. Both B_{472}/B_{513} and B_{472}/B_{560} ratios decrease above 2000 m, while

279   B_{472}/B_{438} increases. As mentioned above, such behavior can be an indication that contribution of

280   smoke rises with height.

281   Normalized fluorescence spectra for two height intervals, 1000-1500 m and 2500-3000 m

282   are shown in Fig.11c. In the second interval, the spectrum is shifted towards longer wavelengths,

283   which corroborates that smoke fraction in the aerosol mixture increases above 2000 m. Thus, the

284   analysis of this episode demonstrates that multi-spectral fluorescence backscattering provides

285   opportunity for particle identification even in the presence of hygroscopic growth.

286

287   **Conclusions and perspectives**

288   Observations performed with a five-channel fluorescence lidar allow estimation of

289   atmospheric aerosol fluorescence spectrum. For urban aerosol type the maximum of fluorescence

290   is observed at 472 nm. However, for smoke particles, the maximum is shifted toward longer

291   wavelengths and the fluorescence backscattering coefficients in the 472 nm, 513 nm and 560 nm

292   channels are comparable. Hence, the ratios B_{472}/B_{513} or B_{472}/B_{560}, allow identification of the

293   smoke layers because, for smoke, these ratios are smaller than for urban particles.

294   During strong forest fires in August 2022 we regularly observed over Moscow aerosol

295   plumes, characterized by high fluorescence capacity ($G_{472} > 1.0 \times 10^{-4}$). Inside these plumes, lidar

296   ratio S_{355} increased up to 60 sr simultaneously with a shift of the fluorescence maximum to 513

297   nm or 560 nm. Particles inside plume are very likely composed of "pure" smoke, while outside

298   the plume, a smoke/urban mixture is probable. Classification of aerosol particles based on single

299   channel fluorescence measurements has limitations at high RH because the fluorescence capacity

300   is decreasing due to water uptake. However, our experimental database of fluorescence

301   backscattering ratios does not show noticeable dependence with RH, which means these ratios

302   allow us to identify smoke layers even in the presence of hygroscopic growth.

303   In our measurements, the laser emitted only 355 nm radiation. However, such

304   configuration is not optimum for aerosol characterization: it is important to use dual-wavelength

305   (355, 532 nm) depolarization and lidar ratio measurements together with the fluorescence

306   observations. Such Laser Induced Fluorescence Exploratory instrument (LIFE) is currently under

307   construction and will start operation in 2023, at LOA, ATOLL platform (France), in the frame of

308   the OBS4CLIM project and AGORA-Lab research and development activities. More generally,

309 it seems promising to upgrade widely-used multiwavelength Mie-Raman high performance lidars
310 with a couple of fluorescence channels. According to our results, at least for smoke, the 472 nm
311 and 513 nm channels can be considered. The wavelengths of aniti-Stokes components of
312 nitrogen and oxygen stimulated by 532 nm radiation are 473 nm and 491 nm respectively. The
313 oxygen component is blocked by the filter, while the nitrogen one is inside the transmission band
314 of the 472 nm channel. The power of anti-Stokes scattering increases with temperature, but even
315 at $30C^0$ its contribution to the fluorescence signal is insignificant. Estimations show that for
316 backscattering coefficient $\beta_{355}=1.0$ $Mm^{-1}sr^{-1}$ and $\beta_{F513}=0.2\times10^{-4}$ $Mm^{-1}sr^{-1}$ (urban aerosol), the
317 relative contribution of the nitrogen anti-Stokes component to the fluorescence (the fraction of
318 β_{F472}) at 1000 m height is below 4×10^{-4}.

319 The results presented in this study are preliminary. We focused mainly on the fresh
320 smoke analysis. However, smoke particle fluorescence properties depend on its chemical
321 composition, in particular, on its organic carbon fraction. In addition, smoke fluorescence may
322 be influenced by the burning process and transportation conditions. More observation
323 campaigns, at different locations, are needed to clarify this. In the coming Spring – Summer
324 period analysis of fluorescence spectra of different aerosol types, in particular, the pollens, is
325 planned. At present, the system used in this study is being modified to include depolarization
326 capability.

327

328 *Data availability*. Lidar measurements are available upon request
329 (philippe.goloub@univ-lille.fr).
330
331 *Author contributions*. IV assembled the lidar and wrote the paper. NK and MK performed the
332 measurements. QH, and PG analyzed data and helped with paper preparation. TP helped with
333 lidar design, DL participated in paper preparation.
334 .
335 *Competing interests*. The authors declare that they have no conflict of interests.

336

337 **Acknowledgement**
338 Development of the lidar system was supported by Russian Science Foundation (project
339 21-17-00114). We acknowledge funding from the CaPPA project funded by the ANR through
340 the PIA under contract ANR-11-LABX-0005-01, the "Hauts de France" Regional Council
341 (project CLIMIBIO) and the European Regional Development Fund (FEDER). ESA/QA4EO

342   program is greatly acknowledged for support of observation activity at LOA as well as

343   OBS4CLIM Equipex project funded by ANR.

344

References

345 **References**

346 Adam, M., Nicolae, D., Stachlewska, I. S., Papayannis, A., and Balis, D.: Biomass burning

347   events measured by lidars in EARLINET – Part 1: Data analysis methodology, Atmos. Chem.

348   Phys., 20, 13905–13927, https://doi.org/10.5194/acp-20-13905-2020, 2020.

349 Ansmann, A., Riebesell, M., Wandinger, U., Weitkamp, C., Voss, E., Lahmann, W., and

350   Michaelis, W.: Combined Raman elastic-backscatter lidar for vertical profiling of moisture,

351   aerosols extinction, backscatter, and lidar ratio, Appl.Phys.B, *55*, 18-28, 1992.

352 Boucher, O., Randall, D., Artaxo, P., Bretherton, C., Feingold, G., Forster, P., Kerminen, V.-M.,

353   Kondo, Y., Liao, H., Lohmann, U., Rasch, P., Satheesh, S. K., Sherwood, S., Stevens, B., and

354   Zhang, X. Y.: Clouds and Aerosols, in: Climate Change 2013: The Physical Science Basis.

355   Contribution of Working Group I to the Fifth Assessment Report of the Intergovernmental

356   Panel on Climate Change, edited by: Stocker, T. F., Qin, D., Plattner, G.-K., Tignor, M.,

357   Allen, S. K., Boschung, J., Nauels, A., Xia, Y., Bex, V., and Midgley, P.,M., Cambridge

358   University Press, Cambridge, United Kingdom and New York, NY, USA, 2013

359 Burton, S. P., Ferrare, R. A., Hostetler, C. A., Hair, J.W., Rogers, R. R., Obland, M. D., Butler,

360   C. F., Cook, A. L., Harper, D. B., and Froyd, K. D.: Aerosol classification using airborne

361   High Spectral Resolution Lidar measurements – methodology and examples, Atmos. Meas.

362   Tech., 5, 73–98, 2012. https://doi.org/10.5194/amt-5-73-2012

363 Burton, S. P., Ferrare, R. A., Vaughan, M. A., Omar, A. H., Rogers, R. R., Hostetler, C. A., and

364   Hair, J. W.: Aerosol classification from airborne HSRL and comparisons with the CALIPSO

365   vertical feature mask, Atmos. Meas. Tech., 6, 1397–1412, 2013. https://doi.org/10.5194/amt-

366   6-1397-2013

367 Dubovik, O., Holben, B. N., Eck, T. F., Smirnov, A., Kaufman, Y. J., King, M. D., Tanre, D.,

368   and Slutsker, I.: Variability of absorption and optical properties of key aerosol types observed

369   in worldwide locations, J. Atmos. Sci., 59, 590–608, 2002.

370 Groß, S., Esselborn, M., Weinzierl, B., Wirth, M., Fix, A., and Petzold, A.: Aerosol classification

371   by airborne high spectral resolution lidar observations, Atmos. Chem. Phys., 13, 2487–2505,

372   2013. https://doi.org/10.5194/acp-13-2487-2013

373 Hara, Y., Nishizawa, T., Sugimoto , N., Osada, K., Yumimoto, K., Uno, I., Kudo, R., and

374   Ishimoto, H.: Retrieval of aerosol components using multi-wavelength Mie-Raman lidar and

comparison with ground aerosol sampling, Remote Sens., 10, 937, 2018. https://doi:10.3390/rs10060937

Hu, Q., Goloub, P., Veselovskii, I., and Podvin, T.: The characterization of long-range transported North American biomass burning plumes: what can a multi-wavelength Mie-Raman-polarization-fluorescence lidar provide? Atmos. Chem. Phys. 22, 5399–5414, 2022 https://doi.org/10.5194/acp-22-5399-2022

Knippers,W., van Helvoort, K., and Stolte, S.: Vibrational overtones of the homonuclear diatomics (N2, O2, D2) observed by the spontaneous 385 Raman effect, Chem. Phys. Let., 121, 279–286, 1985. https://doi.org/10.1016/0009-2614(85)87179-7

Mamouri, R.-E., and Ansmann, A.: Potential of polarization/Raman lidar to separate fine dust, coarse dust, maritime, and anthropogenic aerosol profiles, Atmos. Meas. Tech., 10, 3403–3427, 2017. https://doi.org/10.5194/amt-10-3403-2017

Mylonaki, M., Giannakaki, E., Papayannis, A., Papanikolaou, C.-A., Komppula, M., Nicolae, D., Papagiannopoulos, N., Amodeo, A., Baars, H., and Soupiona, O.: Aerosol type classification analysis using EARLINET multiwavelength and depolarization lidar observations, Atmos. Chem. Phys., 21, 2211–2227, 2021. https://doi.org/10.5194/acp-21-2211-2021

Nicolae, D., Vasilescu, J., Talianu, C., Binietoglou, I., Nicolae, V., Andrei, S., and Antonescu, B.: A neural network aerosol-typing algorithm based on lidar data, Atmos. Chem. Phys., 18, 14511–14537, 2018. https://doi.org/10.5194/acp-18-14511-2018

Papagiannopoulos, N., Mona, L., Amodeo, A., D'Amico, G., Gumà Claramunt, P., Pappalardo, G., Alados-Arboledas, L., Guerrero- Rascado, J. L., Amiridis, V., Kokkalis, P., Apituley, A., Baars, H., Schwarz, A.,Wandinger, U., Binietoglou, I., Nicolae, D., Bortoli, D., Comerón, A., Rodríguez-Gómez, A., Sicard, M., Papayannis, A., and Wiegner, M.: An automatic observation-based aerosol typing method for EARLINET, Atmos. Chem. Phys., 18, 15879–15901, 2018. https://doi.org/10.5194/acp-18-15879-2018

Reichardt, J., Behrendt, O., and Lauermann, F.: Spectrometric fluorescence and Raman lidar: absolute calibration of aerosol fluorescence spectra and fluorescence correction of humidity measurements, Atmos. Meas. Tech., 16, 1–13, 2023. https://doi.org/10.5194/amt-16-1-2023

Saito,Y., Hosokawa, T., Shiraishi, K.: Collection of excitation-emission-matrix fluorescence of aerosol-candidate-substances and its application to fluorescence lidar monitoring, Appl. Opt., 61, 653 – 660, 2022.

406 Sugimoto, N., Huang, Z., Nishizawa, T., Matsui, I., Tatarov, B.: Fluorescence from atmospheric
407   aerosols observed with a multichannel lidar spectrometer," Opt. Expr. 20, 20800-20807, 2012.
408 Venable, D. D., Whiteman, D. N., Calhoun, M. N., Dirisu, A.O., Connell, R. M., Landulfo, E.:
409   Lamp mapping technique for independent determination of the water vapor mixing ratio
410   calibration factor for a Raman lidar system, Appl. Opt., 50, 4622 - 4632, 2011.
411 Veselovskii, I., Griaznov, V., Kolgotin, A., Whiteman, D.: "Angle- and size-dependent
412   characteristics of incoherent Raman and fluorescent scattering by microsoheres 2.: Numerical
413   simulation", Appl. Opt. 41, 5783-5791, 2002
414 Veselovskii, I., Hu, Q., Goloub, P., Podvin, T., Korenskiy, M., Pujol, O., Dubovik, O., Lopatin,
415   A.: Combined use of Mie-Raman and fluorescence lidar observations for improving aerosol
416   characterization: feasibility experiment, Atm. Meas. Tech., 13, 6691–6701, 2020.
417   doi.org/10.5194/amt-13-6691-2020.
418 Veselovskii, I., Hu, Q., Goloub, P., Podvin, T., Choël, M., Visez, N., and Korenskiy, M.: Mie–
419   Raman–fluorescence lidar observations of aerosols during pollen season in the north of
420   France, Atm. Meas. Tech., 14, 4773–4786, 2021. doi.org/10.5194/amt-14-4773-2021
421 Veselovskii, I., Hu, Q., Ansmann, A., Goloub, P., Podvin, T., Korenskiy, N.: Fluorescence lidar
422   observations of wildfire smoke inside cirrus: A contribution to smoke-cirrus - interaction
423   research, Atmos. Chem. Phys., 22, 5209–5221, 2022a. https://doi.org/10.5194/acp-22-5209-
424   2022a.
425 Veselovskii, I., Hu, Q., Goloub, P., Podvin, T., Barchunov, B., and Korenskii, M.: Combining
426   Mie–Raman and fluorescence observations: a step forward in aerosol classification with lidar
427   technology, Atmos. Meas. Tech., 15, 4881–4900, 2022b. https://doi.org/10.5194/amt-15-
428   4881-2022.
429 Wang, N., Shen, X., Xiao, D., Veselovskii, I., Zhao,C., Chen, F., Liu, C., Rong, Y., Ke, J., Wang,
430   B., Qi, B., Liu, D.: Development of ZJU high-spectral-resolution lidar for aerosol and cloud:
431   feature detection and classification, Journal of Quantitative Spectroscopy & Radiative
432   Transfer, v.261, 107513, 2021. doi.org/10.1016/j.jqsrt.2021.107513
433
434

435

436
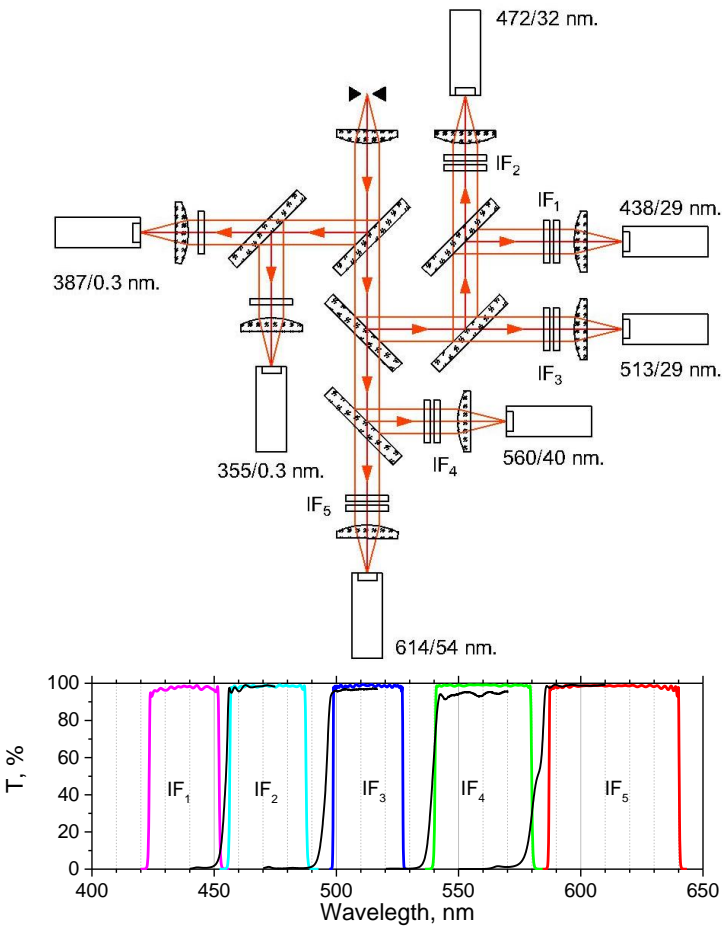
Fig.1. Optical scheme of the receiving module of the lidar together with transmissions of interference filters IF$_1$-IF$_5$ in the fluorescence channels. Black lines show the transmissions of the 45 degree dichroic beam splitters used for separation of fluorescence spectral components.

440

441

442

443

444

445
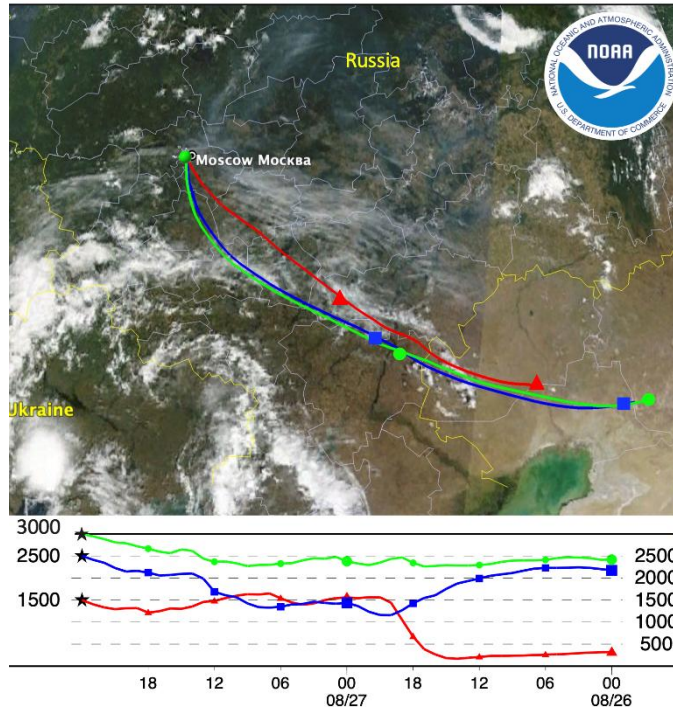
Fig.2. Two-day backward trajectories from the NOAA HYSPLIT model for the air mass in Moscow on 28 August at 00:00 UTC. The basemap is the Earth's true color image observed by MODIS Terra for the same period.

449

450

451

452

453

454
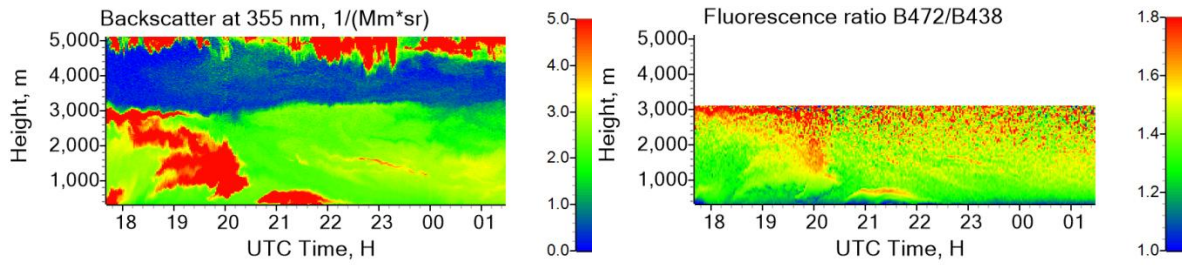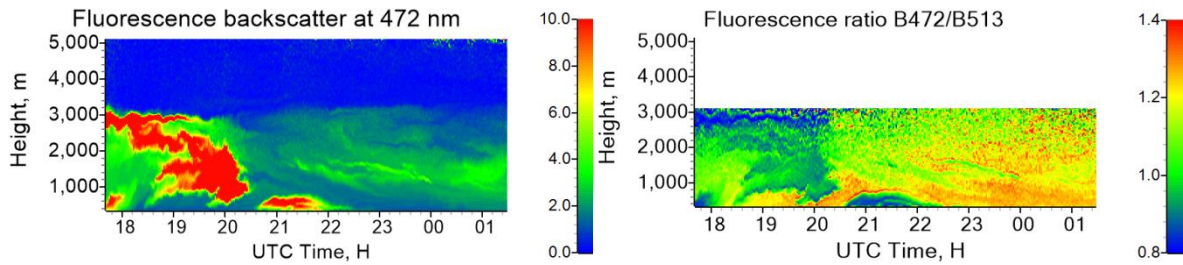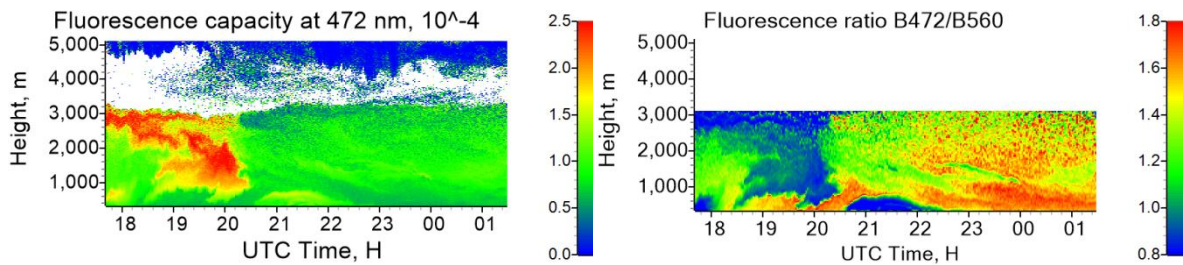
Fig.3. Spatio – temporal distribution of particle parameters on the night 27-28 August 2022. (left column) Aerosol backscattering coefficient β_{355}, fluorescence backscattering β_{F472} (in 10^{-4} Mm^{-1}sr^{-1}), fluorescence capacity G_{472}. (right column) Ratios of fluorescence spectral backscattering coefficients B_{472}/B_{438}, B_{472}/B_{513}, B_{472}/B_{560}.

459

460
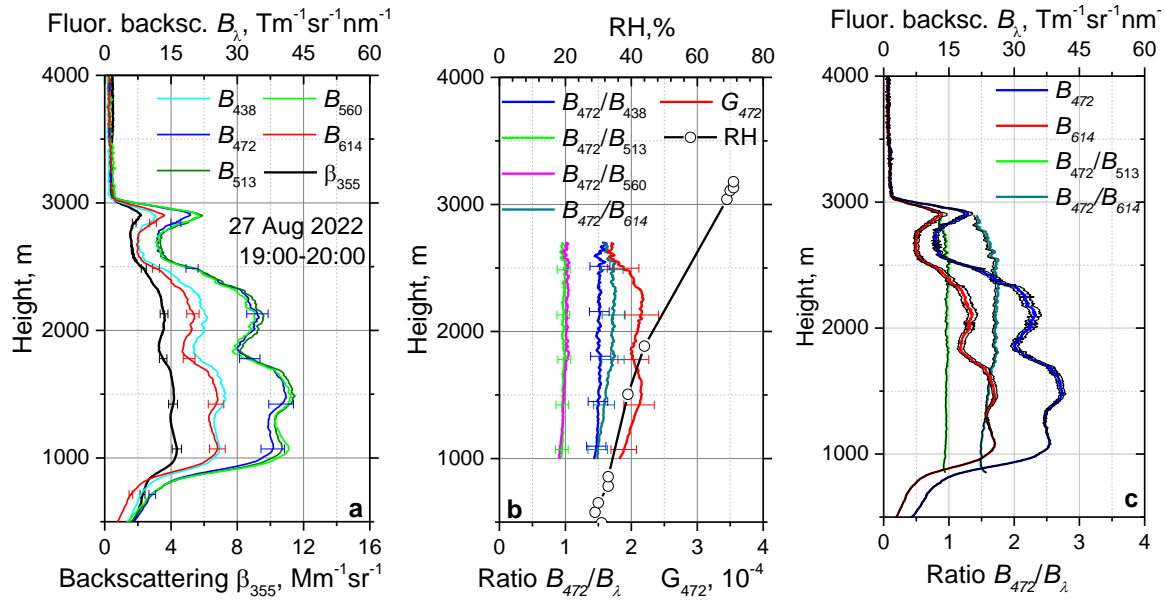
461

462 Fig.4. Observations on 27 August 2022 for period 19:00-20:00 UTC. (a) Fluorescence spectral

463 backscattering coefficients B_λ at 438, 472, 513, 560, 614 nm and the aerosol backscattering

464 coefficient β_{355}. (b) The ratios B_{472}/B_{438}, B_{472}/B_{513}, B_{472}/B_{560}, B_{472}/B_{614} and the fluorescence

465 capacity G_{472}. Symbols show the relative humidity measured by a radiosonde at 00:00 UTC on

466 28 August. (c) Fluorescence spectral backscattering coefficients B_λ at 472, 614 nm wavelengths

467 and the ratios B_{472}/B_{513}, B_{472}/B_{614} calculated for the Angstrom exponent values A=0.5, 1, 1.5.

468 Results for A=0.5, 1.5 are shown with thin black lines, the increase of A decreases the B_λ. The

469 profiles at plots (a, b) are calculated for A=1.

470

471
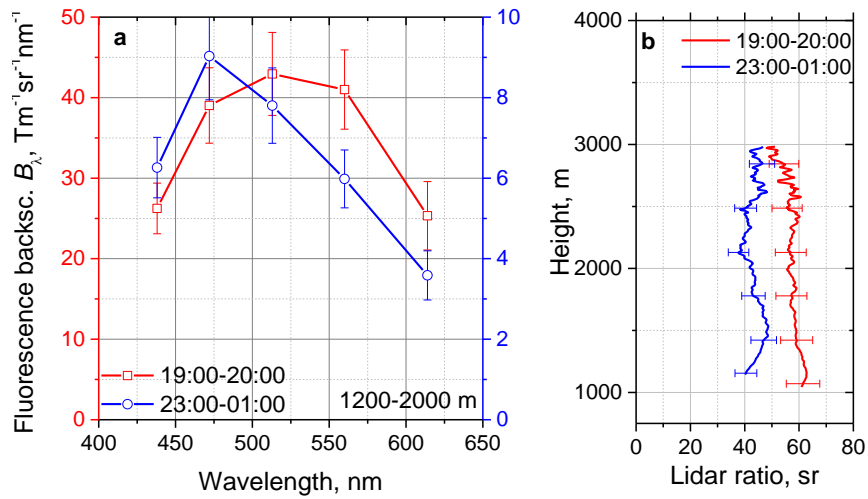
472

473   Fig.5. (a) Spectrum of fluorescence backscattering B_λ on the night 27-28 August 2022 for 19:00-

474   20:00 and 23:00-01:00 UTC intervals. Results are averaged inside 1200-2000 m height range. (b)

475   Profiles of lidar ratios at 355 nm for the same temporal intervals.

476

477
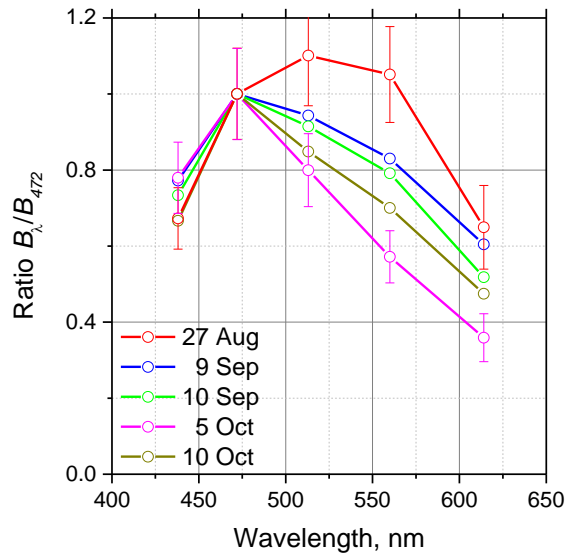
478

479   Fig.6. Fluorescence spectra measured in September - October 2022, when forest fires were over.

480   Fluorescence backscattering coefficients B_λ were averaged inside $500 - 1000$ m height range and

481   normalized on B_{472}. For comparison, the fluorescence spectrum in smoke plume on 27 August

482   from Fig.5 is also presented.

483

484
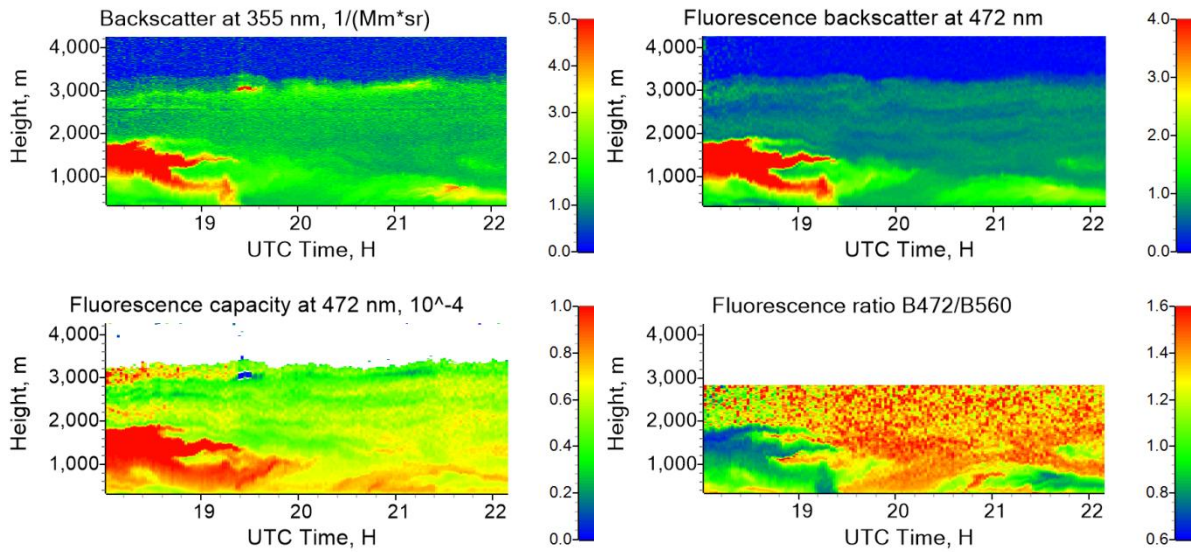
Fig.7. Observations on 17 August 2022. (left column) Aerosol backscattering coefficient β_{355} and fluorescence capacity G_{472}. (right column) Fluorescence backscattering coefficient β_{F472} (in 10^{-4} $Mm^{-1}sr^{-1}$) and the ratio of fluorescence spectral backscattering coefficients B_{472}/B_{560}.
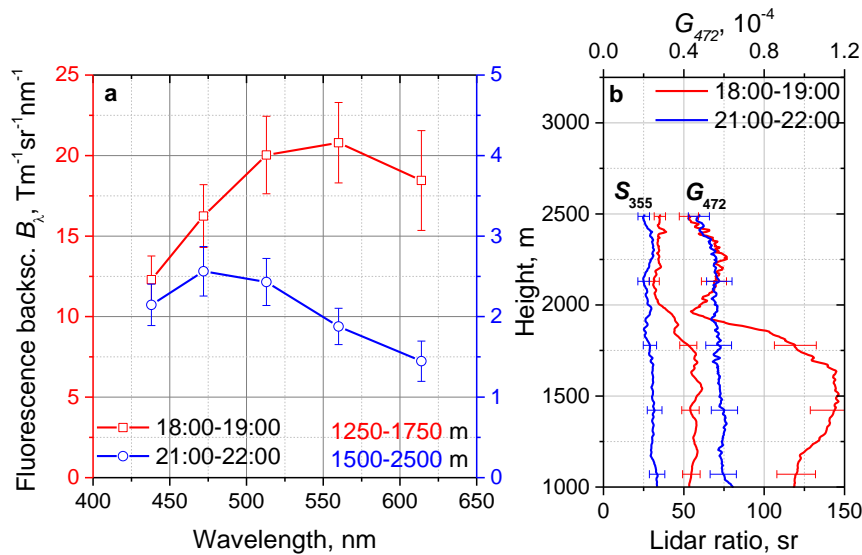
Fig.8. (a) Spectra of fluorescence backscattering B_λ on 17 August 2022 for 18:00-19:00 UTC and 21:00-22:00 UTC periods. Results are averaged within 1250-1750 m and 1500-2500 m height ranges respectively. (b) Profiles of lidar ratio S_{355} and fluorescence capacity G_{472} for the same temporal periods.

498
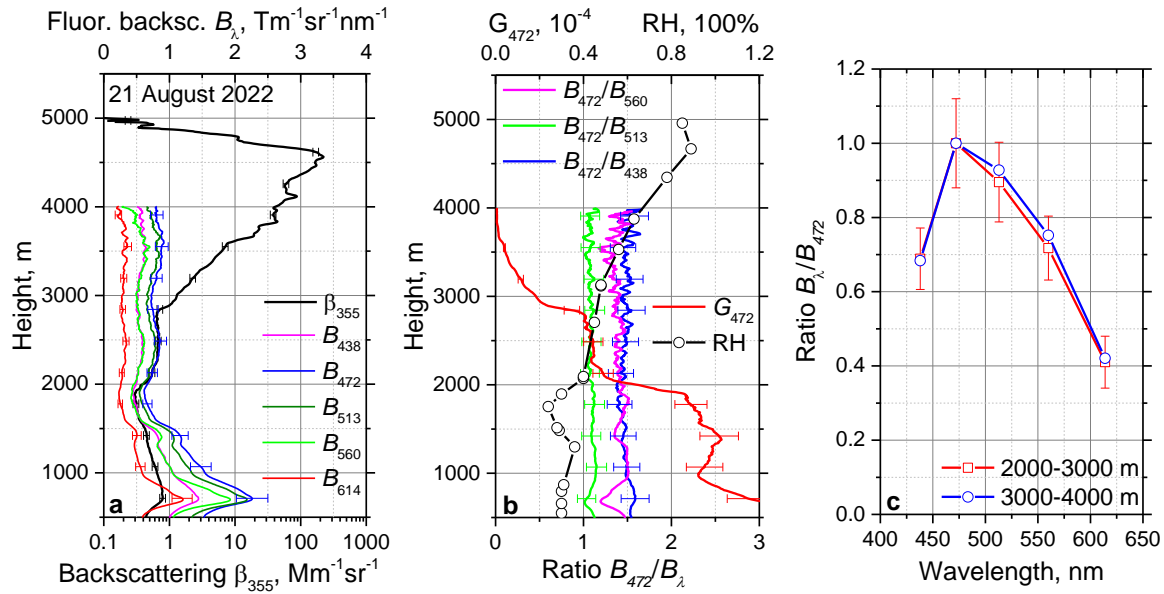
Fig.9. Vertical profiles of the particle parameters on 21 August 2022 for period 22:00-24:00 UTC. (a) The fluorescence spectral backscattering coefficients B_λ at 438, 472, 513, 560, 614 nm and the aerosol backscattering coefficient β_{355}. (b) The ratios B_{472}/B_{438}, B_{472}/B_{513}, B_{472}/B_{560} and the fluorescence capacity G_{472}. Symbols show the relative humidity measured by a radiosonde at 00:00 UTC on 22 August. (c) Spectrum of the fluorescence backscattering coefficient B_λ for height intervals 2000-3000 m and 3000-4000 m. Values of B_λ are normalized on B_{472}.

505

506

507
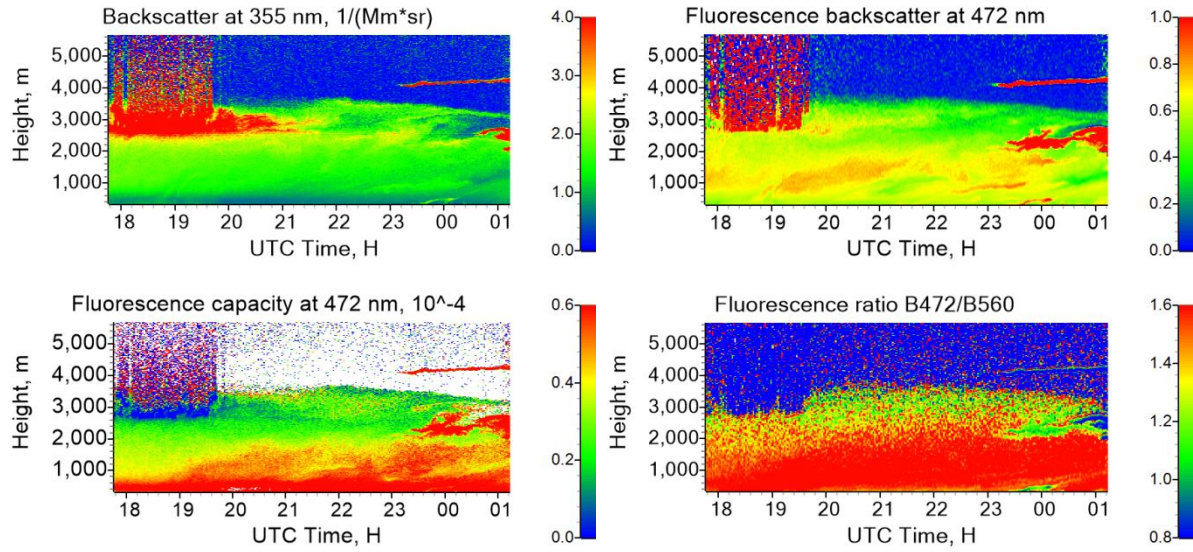
508

509 Fig.10. Spatio-temporal distributions of the particle parameters on the night 23-24 August 2022.

510 (left column) The aerosol backscattering coefficient β_{355} together with the fluorescence capacity

511 G_{472}. (right column) The fluorescence backscattering coefficient β_{F472} (in 10^{-4} $Mm^{-1}sr^{-1}$) and the

512 ratio B_{472}/B_{560}.

513

514
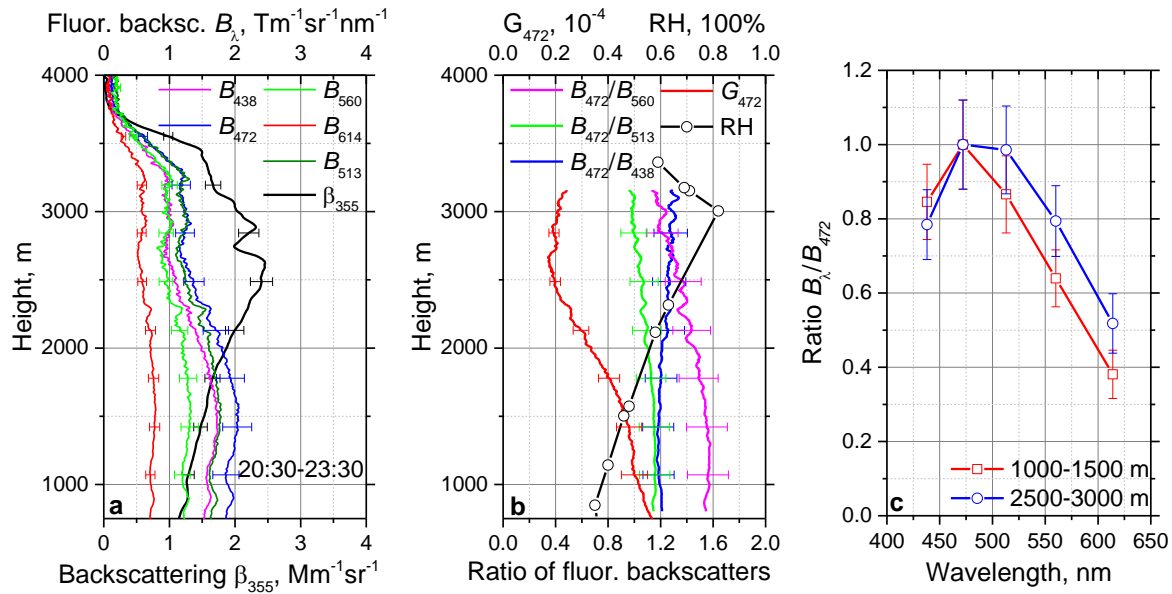
518 Fig.11. Vertical profiles of the particle parameters on 23 August 2022 for period 20:30-23:30

519 UTC. (a) The fluorescence spectral backscattering coefficients B_λ at 438, 472, 513, 560, 614 nm

520 and the aerosol backscattering coefficient β_{355}. (b) The ratios B_{472}/B_{438}, B_{472}/B_{513}, B_{472}/B_{560} and

521 the fluorescence capacity G_{472}. Symbols show the relative humidity measured by a radiosonde at

522 00:00 UTC on 24 August. (c) Spectrum of the fluorescence backscattering coefficient B_λ for

523 height intervals 1000-1500 m and 2500-3000 m. Values of B_λ are normalized on B_{472}.

524

525